



Transition in a 2-D lid-driven cavity flow

Yih-Ferng Peng^a, Yuo-Hsien Shiau^b, Robert R. Hwang^{b,*}

^a *Department of Civil Engineering, National Chi Nan University, Taiwan, ROC*

^b *Institute of Physics, Academia Sinica, Taipei 11529, Taiwan, ROC*

Received 16 August 2000; received in revised form 16 May 2001; accepted 16 August 2001

Abstract

Direct numerical simulations about the transition process from laminar to chaotic flow in square lid-driven cavity flows are considered in this paper. The chaotic flow regime is reached after a sequence of successive supercritical Hopf bifurcations to periodic, quasi-periodic, inverse period-doubling, period-doubling, and chaotic self-sustained flow regimes. The numerical experiments are conducted by solving the 2-D incompressible Navier–Stokes equations with increasing Reynolds numbers (Re). The spatial discretization consists of a seventh-order upwind-biased method for the convection term and a sixth-order central method for the diffusive term. The numerical experiments reveal that the first Hopf bifurcation takes place at Re equal to $7402 \pm 4\%$, and a consequent periodic flow with the frequency equal to 0.59 is obtained. As Re is increased to 10,300, a new fundamental frequency (FF) is added to the velocity spectrum and a quasi-periodic flow regime is reached. For slightly higher Re (10,325), the new FF disappears and the flow returns to a periodic regime. Furthermore, the flow experiences an inverse period doubling at $10,325 < Re < 10,700$ and a period-doubling regime at $10,600 < Re < 10,900$. Eventually, for flows with Re greater than 11,000, a scenario for the onset of chaotic flow is obtained. The transition processes are illustrated by increasing Re using time–velocity histories, Fourier power spectra, and the phase–space trajectories. In view of the conducted grid independent study, the values of the critical Re presented above are estimated to be accurate within $\pm 4\%$. © 2002 Elsevier Science Ltd. All rights reserved.

Keywords: Transition; Cavity flow; Direct numerical simulation

1. Introduction

For a long time, people have been interested in the transition process from laminar to the chaotic flow. Nowadays, the chaotic theory is dramatically developed and the sequence of the

* Corresponding author. Tel.: +886-2-27899646; fax: +886-2-27834187.

E-mail addresses: phhwang@ccvax.sinica.edu.tw, phhwang@phys.sinica.edu.tw (R.R. Hwang).

ordered transition process is verified [1–4]. Experimental studies in the context of transition to chaotic flow have been proceeded for over 30 years. In closed system flows like Reyleigh–Benard convection [5,6] and Taylor–Couette flow [7,8], a sequence of ordered transitions has been verified experimentally. The process from a predictable flow to an unpredictable, but deterministic, chaotic regime has also been studied by numerical approaches. Numerical simulations have successfully been performed in flows such as Reyleigh–Benard convection [9], plane, and modified channel flows [10–13]. With the advent of high-speed computers, numerical simulations have received increasing acceptance as a practical method in exploring the transition process. It is in this light that we have stimulated to investigate the transition process numerically in a fundamental flow—a 2-D square lid-driven cavity flow.

Research concerning the structure of lid-driven cavity flows is an area of continuing interest and was regarded as a benchmark study in some major international workshops. This classical problem has attracted considerable attentions because its flow configuration is relevant to many industrial applications. It is the geometrical simplicity that facilitates experimental calibrations or numerical implementations, thus providing benchmark data for comparison and validation. Inside this cavity, however, the flow physics is by no means simple. Several flow characteristics which prevail in processing industries, such as boundary layers, eddies of different size and characteristics and various instabilities, may coexist.

Numerical investigation of the flow physics inside a lid-driven cavity dates back to the pioneering work of Burggraf [14]. Numerical solutions of the steady base flow in a square lid-driven cavity for Reynolds numbers (Re) up to 10,000 have been obtained by several investigators [15–20]. Due to these accurate numerical solutions, the lid-driven cavity flow is considered as the benchmark for the assessment and validation of numerical methods for solving Navier–Stokes equations. However, the stability of the 2-D steady state flow was not explored in those studies. The first bifurcation from steady to periodic flow was investigated for the first time by Poliashenko and Aidun [21]. They showed that the steady state in a lid-driven cavity problem becomes unstable at $Re = 7763 \pm 2\%$. The unsteady lid-driven cavity has also been studied numerically by Nobile [22], but the transition process and chaotic phenomena were not investigated.

Recently, Cazemier et al. [23] studied the lid-driven cavity using a proper orthogonal decomposition and low-dimensional models. They found that the first Hopf bifurcation takes place at $Re = 7819$ and the stable periodic-flow regimes are located between $7819 < Re < 8200$, $8400 < Re < 11,188$, and $11,500 < Re < 11,900$. For the two interesting intervals, $8200 < Re < 8400$ and $11,188 < Re < 11,500$, flows are quasi-periodic. Cazemier et al. [23] have also investigated the lid-driven cavity flow numerically at some selected Re , but their limited direct numerical simulation (DNS) results seem to not confirm the complicated transitions of their dynamic system. In recognition of this, we feel that serial numerical investigations are required to broaden our understanding of the complex transitions in a lid-driven cavity. As a result, we propose a DNS study of the transition of lid-driven cavity flow by increasing the Re .

This paper is organized as follows. In Section 2, we begin with the introduction of the equations of fluid motion for the incompressible 2-D case. Subsequently, the boundary conditions are briefly described. In Section 3, the finite difference discretization method, together with the segregated solution algorithm, is described. As an analysis tool, we validate the applicability of the employed computer code in simulating the steady base flow within a lid-driven cavity by carrying out a comparison test. In Section 4, we report the results of the numerical simulations in terms of

time–velocity histories, Fourier power spectrum, and phase–space trajectories for increasing Re from subcritical to supercritical flow regimes. In Section 5, we present the conclusions of this study.

2. Problem formulation

We consider 2-D, incompressible flows in a square lid-driven cavity. In the absence of body forces, the working dimensionless equations permitting the analysis of viscous fluid flows take the following form for a given Re :

$$\frac{\partial u}{\partial x} + \frac{\partial v}{\partial y} = 0, \quad (1)$$

$$\frac{\partial u}{\partial t} + u \frac{\partial u}{\partial x} + v \frac{\partial u}{\partial y} = -\frac{\partial p}{\partial x} + \frac{1}{Re} \left(\frac{\partial^2 u}{\partial x^2} + \frac{\partial^2 u}{\partial y^2} \right), \quad (2)$$

and

$$\frac{\partial v}{\partial t} + u \frac{\partial v}{\partial x} + v \frac{\partial v}{\partial y} = -\frac{\partial p}{\partial y} + \frac{1}{Re} \left(\frac{\partial^2 v}{\partial x^2} + \frac{\partial^2 v}{\partial y^2} \right), \quad (3)$$

where u and v are the velocity components in x and y directions, respectively, p is the static pressure, Re is the Reynolds number defined as $Re = U_0 D / \nu$, and ν is the kinematic viscosity. In Fig. 1, the height of the cavity, D , and lid-driven velocity, U_0 , are specified as the unit length and velocity. Time and pressure are normalized by D/U_0 and ρU_0^2 , respectively. Boundary conditions

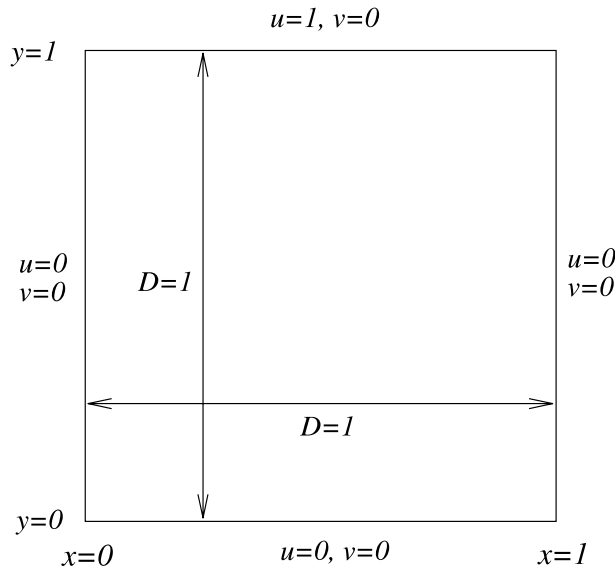


Fig. 1. Cavity flow configuration, coordinates, and boundary conditions.

for the velocity field are the lid-driven velocity at the roof-wall and no-slip conditions for velocity components at the bottom-wall and two side walls. They are:

$$u = 1, \quad v = 0 \quad \text{at } y = 1, \quad (4)$$

$$u = v = 0 \quad \text{at } y = 0, \quad x = 0, \quad \text{and } x = 1. \quad (5)$$

3. Numerical method

Although in the literature there exist several sets of working variables. We prefer employing the most popular primitive variable formulation for this class of flows, because this setting processes the closure boundary and initial conditions [24]. In as much as the above velocity–pressure formulation is considered, we are faced with choosing a strategy of either grid staggering [25] or collocation [26] to store working variables. While node-to-node pressure oscillations can be alleviated in both grids, we favor the first strategy regardless of programming complications. The rationale behind this choice is based on the fact that we lack a set of indispensable closure boundary conditions for the analysis involving a Poisson-type pressure correction equation. With a staggered grid arrangement, each primitive variable has a node to itself, whereas the pressure node is surrounded by its adjacent velocity component nodes.

When dealing with the primitive variable form of the incompressible Navier–Stokes equations, we encounter two well-known technical difficulties. The first of these is ensuring the satisfaction of discrete divergence-free velocities in an incompressible flow analysis. This constraint condition can be enforced either by using a mixed formulation or by incorporating the incompressibility constraint through the multiple-stage equation. Herein, a partially implicit method, i.e., the marker-and-cell (MAC) method [27,28], is corresponding to the solution of the Poisson pressure equation. The second technical difficulty is the avoidance of numerical instability when a problem of advection dominance is considered. To avoid spurious velocity oscillations and a false diffusion error, which may greatly pollute the flow physics over the entire domain, we advocate the use of a seventh-order-accurate upwind-biased scheme to discretize non-linear advection fluxes.

Briefly, the grid system used for the computation is uniform and staggered. The numerical method employed is based on the MAC method using a second-order-accurate discretization of the conservation of mass and of the pressure gradient, combined with a seventh-order-accurate upwind-biased discretization of the first-order derivative in the advection and a six-order-accurate central discretization of the diffusion. In the case of $u > 0$, the seventh-order upwind scheme [29] discretize the advective flux of $\partial u / \partial x$ by the difference of:

$$\frac{\partial u}{\partial x} = \frac{3u_{i-4,j} - 28u_{i-3,j} + 126u_{i-2,j} - 420u_{i-1,j} + 105u_{i,j} + 252u_{i+1,j} - 42u_{i+2,j} + 4u_{i+3,j}}{420 \Delta h}. \quad (6)$$

The diffusive terms are discretized using a sixth-order-accurate central method [30]. Typically, $\partial^2 u / \partial x^2$ is discretized by the difference of:

$$\frac{\partial^2 u}{\partial x^2} = \frac{2u_{i-3,j} - 27u_{i-2,j} + 270u_{i-1,j} - 490u_{i,j} + 270u_{i+1,j} - 27u_{i+2,j} + 2u_{i+3,j}}{180 \Delta h^2}. \quad (7)$$

Table 1

Location of the primary vortex and velocity components (u and v) at location $(x, y) = (0.6, 0.6)$, for $Re = 5000$

	Primary vortex location	$u(0.6, 0.6)$	$v(0.6, 0.6)$
$\Delta h = 1/40$	(0.51902, 0.53301)	0.02840	−0.03823
$\Delta h = 1/60$	(0.51018, 0.53895)	0.02986	−0.05724
$\Delta h = 1/80$	(0.51302, 0.53607)	0.03712	−0.06215
$\Delta h = 1/100$	(0.51439, 0.53531)	0.04059	−0.06465
$\Delta h = 1/120$	(0.51404, 0.53605)	0.04247	−0.06634
Ref. [15]	(0.5117, 0.5352)	NA	NA
Ref. [22]	(0.5156, 0.5357)	NA	NA

In the neighborhood of all boundaries, smooth transitions from the higher-order methods used in the interior of the computational domain to a second-order method are utilized. Details of the spatial discretizations and the corresponding discretization at boundaries can be found in the study of Wissink [29].

The computations were performed with different mesh resolutions to investigate the adequacy of the spatial discretization. Numerical solutions of a 2-D square lid-driven cavity flow at $Re = 5000$ were resolved for five meshes. The computational locations of the primary vortex and velocity components of u and v at $(x, y) = (0.6, 0.6)$ are collected and listed in Table 1. Computational velocity profiles of the flow with Re equal to 5000 are also obtained and compared to one of the most accurate numerical methods reported [15]. Fig. 2 shows the plots of the profiles of both horizontal velocity along the vertical centerline, and vertical velocity along the horizontal central, obtained on different grids. The present computational velocity profiles with grids 100×100 , and 120×120 are nearly coherent to the fine grid results (256×256) reported by Ghia et al. [15]. This mesh refinement study shows that the numerical solutions of steady cavity flow are approximately independent for $\Delta h \leq 1/100$.

4. Numerical results

We now present numerical results of 2-D flow in the lid-driven cavity. The time evolution of velocity, the power spectra of velocity, and the phase trajectory on $u-v$ plane are shown at a fixed point $(x, y) = (0.6, 0.6)$ of the cavity. It is noted that the fluctuation velocity is small all over the flow field and we chose the point $(0.6, 0.6)$ as a typical example. The solutions in this paper are organized into two branches. The first branch includes the transition from a steady flow to a periodic flow via supercritical Hopf bifurcation and no further bifurcation exists in this branch. The second branch contains more complicated results including quasi-periodic and period-doubling behaviors. The interesting thing is that these two branches consist of bistability. Subsequently, we will give the detailed descriptions of our DNS data.

4.1. The first branch

We examined the transition of the 2-D cavity flow by gradually increasing Re . We found that the steady flow became unstable via a supercritical Hopf bifurcation and was replaced by periodic flow when Re exceeds a threshold value. Herein, we have made a grid refinement study on the first

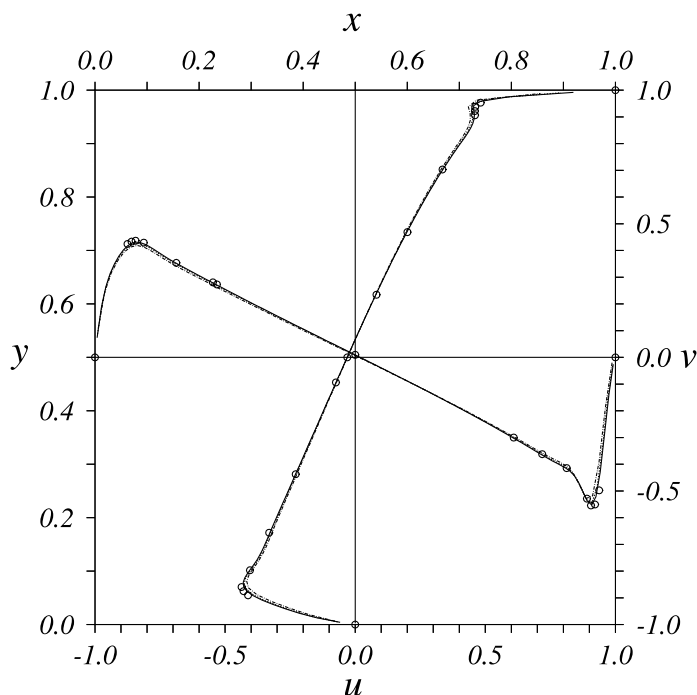


Fig. 2. Computed velocity profiles, for $Re = 5000$. Solid line indicates the present simulations with grid 120×120 , dotted line indicates the present simulations with grid 100×100 , dashed dotted line indicates the present simulations with grid 80×80 , and circle symbol indicates the simulations of Ghia et al. [15] with grid 256×256 .

Hopf bifurcation location based on the 100×100 , 150×150 , and 200×200 grid systems, respectively. The computational results of these grid systems and some previous studies on this topic are revealed in Table 2. In Table 2, the critical Reynolds number (Re_{cr}) where the first Hopf bifurcation takes place for the 100×100 , 150×150 , and 200×200 grid systems are Re equal to 7402, 7694, and 7704, respectively. From the results obtained, it follows that the difference between the Re_{cr} on the 100×100 grid and that on the 150×150 grid is significant, while this difference is negligible when further increasing the grid to 200×200 . And the 150×150 and 200×200 results closely consentient with the previously published work on the topic. From this grid refinement study, it is noted that the first Hopf bifurcation location of 100×100 grid system, i.e. $Re = 7402$, has an error up to 4%. Since the CPU time for computing the cavity flow on 150×150 grids is more than three times of the 100×100 grids and the study on the complex

Table 2
Numerical results of Re_{cr} where the first Hopf bifurcation occurs

	Re_{cr}
This study (100×100)	7402
This study (150×150)	7694
This study (200×200)	7704
Ref. [21]	$7763 \pm 2\%$
Ref. [23]	7819

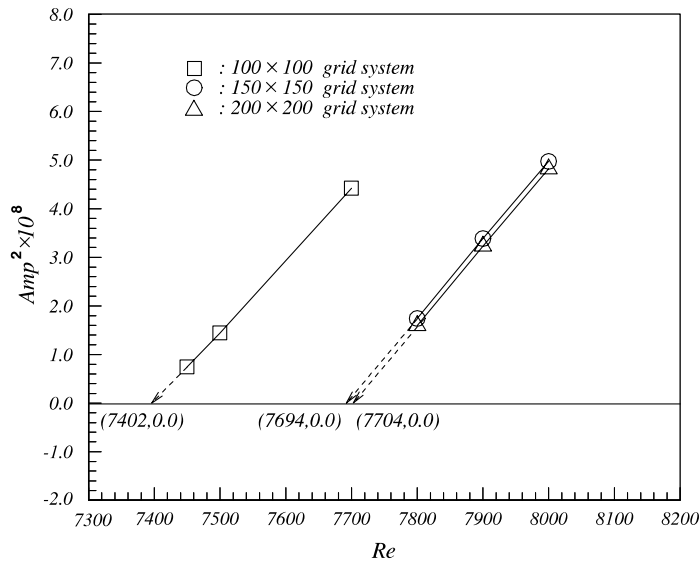


Fig. 3. Plots of the square amplitude of the self-sustained oscillations of u as a function of Re on different grid systems.

transitions requires very large computational efforts, we then adopt the 100×100 grid system to study the transition of the 2-D lid-driven cavity flow for the present study. In terms of the conducted grid independent study, the values of those Re_{cr} where the supercritical bifurcations take place are estimated to be accurate within $\pm 4\%$.

In order to show the characteristic of the Hopf bifurcation, an amplitude parameter A_{mp} is defined as $A_{mp} = \max[u(t)] - \min[u(t)]$, where $\max[u(t)]$ and $\min[u(t)]$ are the maximum and the minimum value of $u(t)$, respectively. In Fig. 3 we plot A_{mp}^2 as a function of Re , where the symbols and the solid lines denote our numerical data and the lines of best fit, respectively. Due to $A_{mp}^2 \propto Re$, we know that the transition from a steady flow to a periodic flow belongs to the standard Hopf bifurcation [12].

For clear visualization of the periodic flow at the first branch, the time evolution of u and v variables, the phase trajectory on $u-v$ plane, and the power spectrum to identify the fundamental frequency (FF) are all demonstrated in Fig. 4. There are two important points about Fig. 4 that need to be discussed. The first point is the appearance of a simple self-sustained oscillation, i.e., the sinusoidal behavior, with the FF equal to 0.59. We call this simple oscillatory structure the “branch-I period-1 pattern” (BIP1P). The second point is that the fluctuation of u (or v) variable is quite small, which is because the main structure in the cavity is unchangeable except the periodic variation of small eddies near to the right corner.

As Re increases, self-sustained oscillatory flows with increasing oscillatory amplitudes and decreasing oscillatory frequencies are obtained. The oscillatory amplitude as a function of Re at the first branch is plotted in Fig. 5. It is seen that there is an inflection point existed around $10,000 < Re < 10,370$. The discontinuous amplitude gradient may imply that there is a supercritical bifurcation. If Re is increased over 10,370 along the first branch solutions, we find that the discontinuous transition appears. It means that BIP1P is replaced by a new structure when Re exceeds 10,370. This kind of sudden change is known to form bistability.

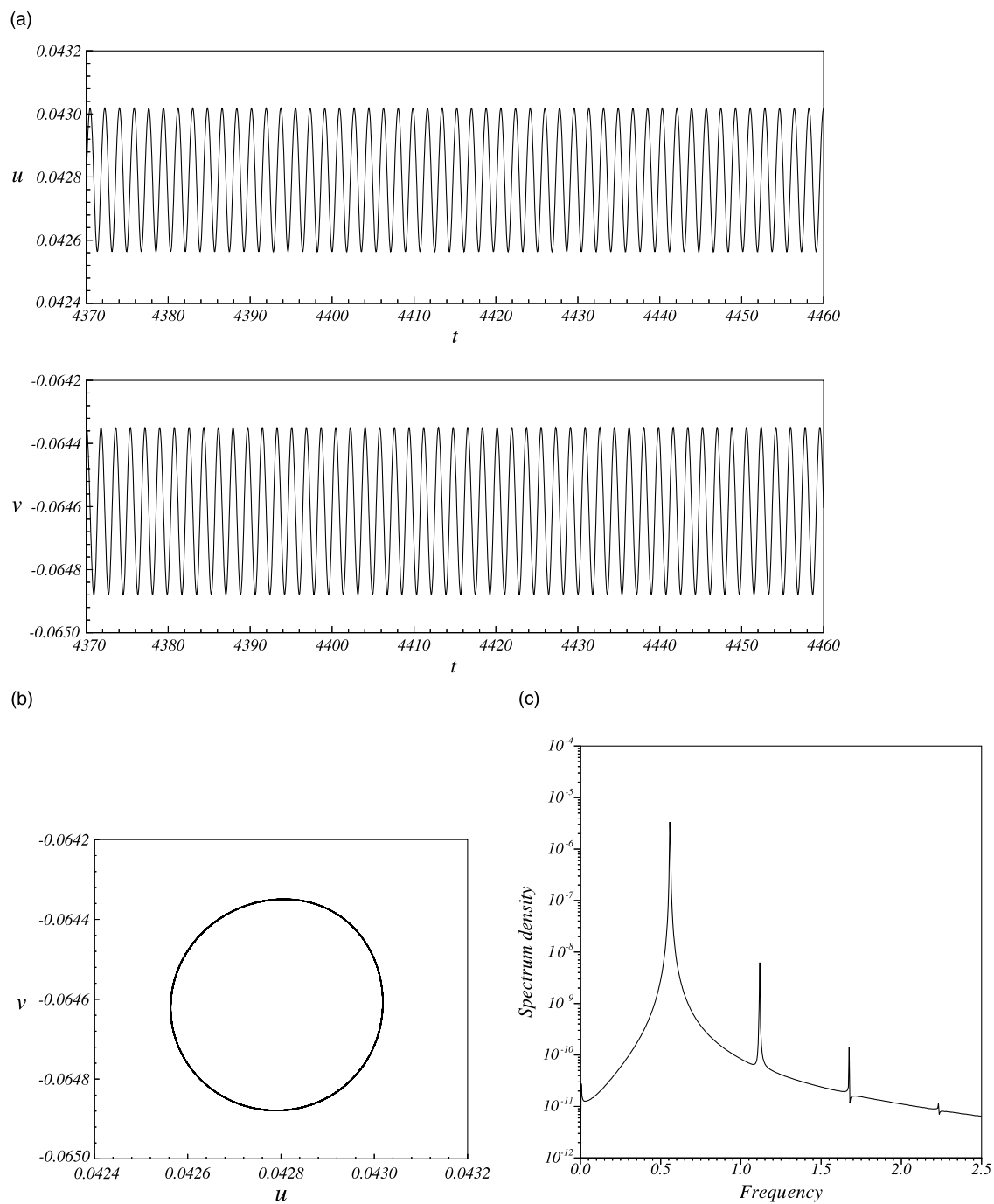


Fig. 4. Computed cavity flow at $Re = 10,200$ (BIP1P). (a) u and v velocities as a function of time t (from $t = 4370$ to $t = 4460$). (b) Phase-space trajectories of v vs. u . (c) Fourier power spectra of the u velocity.

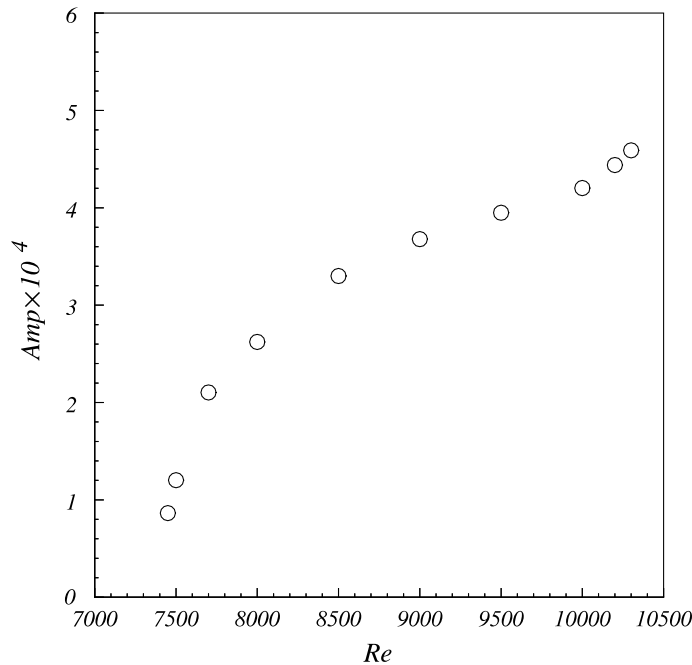


Fig. 5. The amplitude of the oscillations of u as a function of Re along the first branch solutions.

4.2. The second branch

Now we want to show the flow details at the second branch solutions from low Re to high Re . When $Re = 10,300$, the appearance of a quasi-periodic behavior is illustrated in Fig. 6. Two FFs $f_1 = 0.0017$ and $f_2 = 0.069$ can be seen from the analysis of the power spectrum. The ratio between f_1 and f_2 equal to 0.02464 is an irrational number. When $Re = 10,400$, the periodic flow with FF $2f_2$ and its subharmonic frequencies will show up. We call this structure as the “branch-II period-2 pattern” (BIIP2P). The time evolution of $u(t)$ and $v(t)$, the power spectrum, and the phase trajectory on $u-v$ plane of the BIIP2P are plotted in Fig. 7.

When we increase Re to 10,600, the branch-II period-1 pattern with FF f_2 and its harmonics are illustrated in Fig. 8. Note that there are some differences between Figs. 4 and 8, although the two patterns belong to the period-1 structure. The first difference is that the FF is irrelevant. One is $FF = 0.59$ for Fig. 4 and the other is $FF = 0.14$ for Fig. 8. The second is $u(t)$ and $v(t)$ behaviors in Fig. 8(a) are more complicated than in Fig. 4(a). Therefore, we find different period-1 patterns in the lid-driven cavity flow. When Re equals to 10,900, the BIIP2P reappears (see Fig. 9). If we further increase Re , the chaotic pattern can be observed (Fig. 10).

In order to understand the complex configurations of a lid-driven cavity flow clearly, we give the schematic description about the many patterns in this system (Fig. 11). In a simple way, these solutions can be divided into two branches. The first branch includes laminar flow and period-1 pattern. The transition from laminar flow to period-1 pattern is via a supercritical Hopf bifurcation. The second branch includes quasi-periodic, period-1, period-2, and chaotic patterns. The

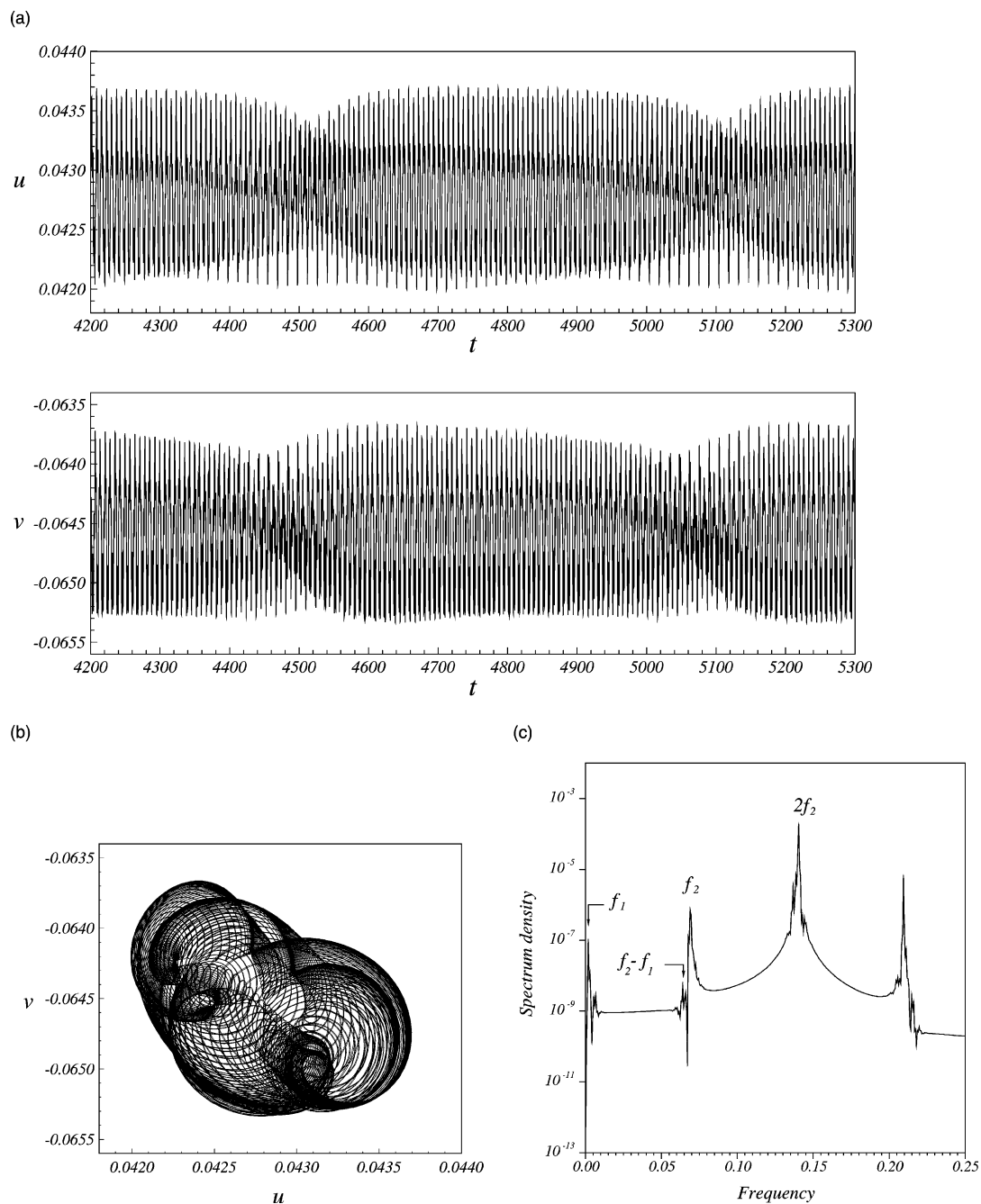


Fig. 6. Computed cavity flow at $Re = 10,300$ (quasi-periodic). (a) u and v velocities as a function of time t (from $t = 4200$ to $t = 5300$). (b) Phase-space trajectories of v vs. u . (c) Fourier power spectra of the u velocity.

transition process in this branch is interesting. For example, the normal (or inverse) period-doubling cascades from period-1 to period-2 pattern (or period-2 to period-1 pattern) and

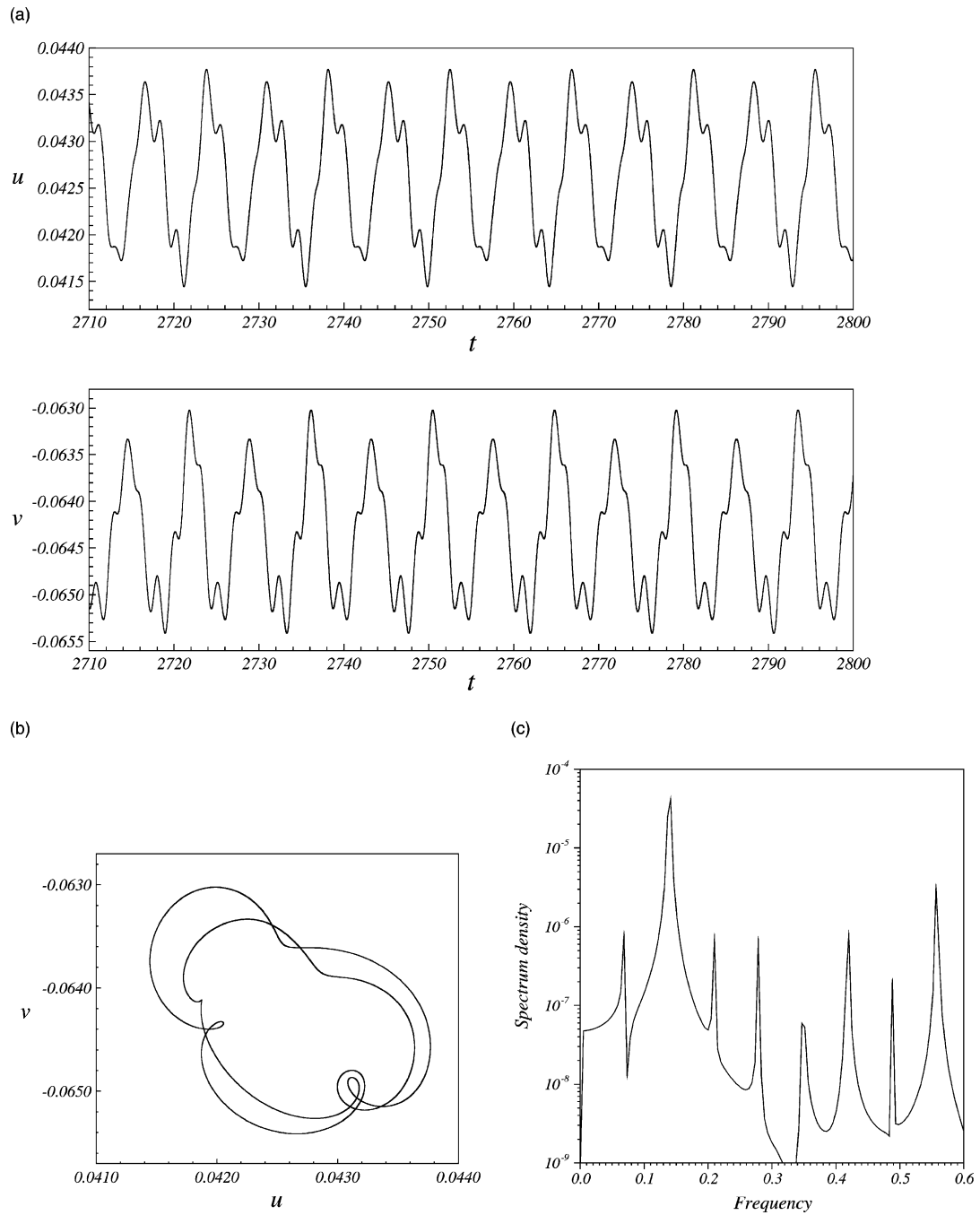


Fig. 7. Computed cavity flow at $Re = 10,400$ (BIIP2P). (a) u and v velocities as a function of time t (from $t = 2710$ to $t = 2800$). (b) Phase-space trajectories of v vs. u . (c) Fourier power spectra of the u velocity.

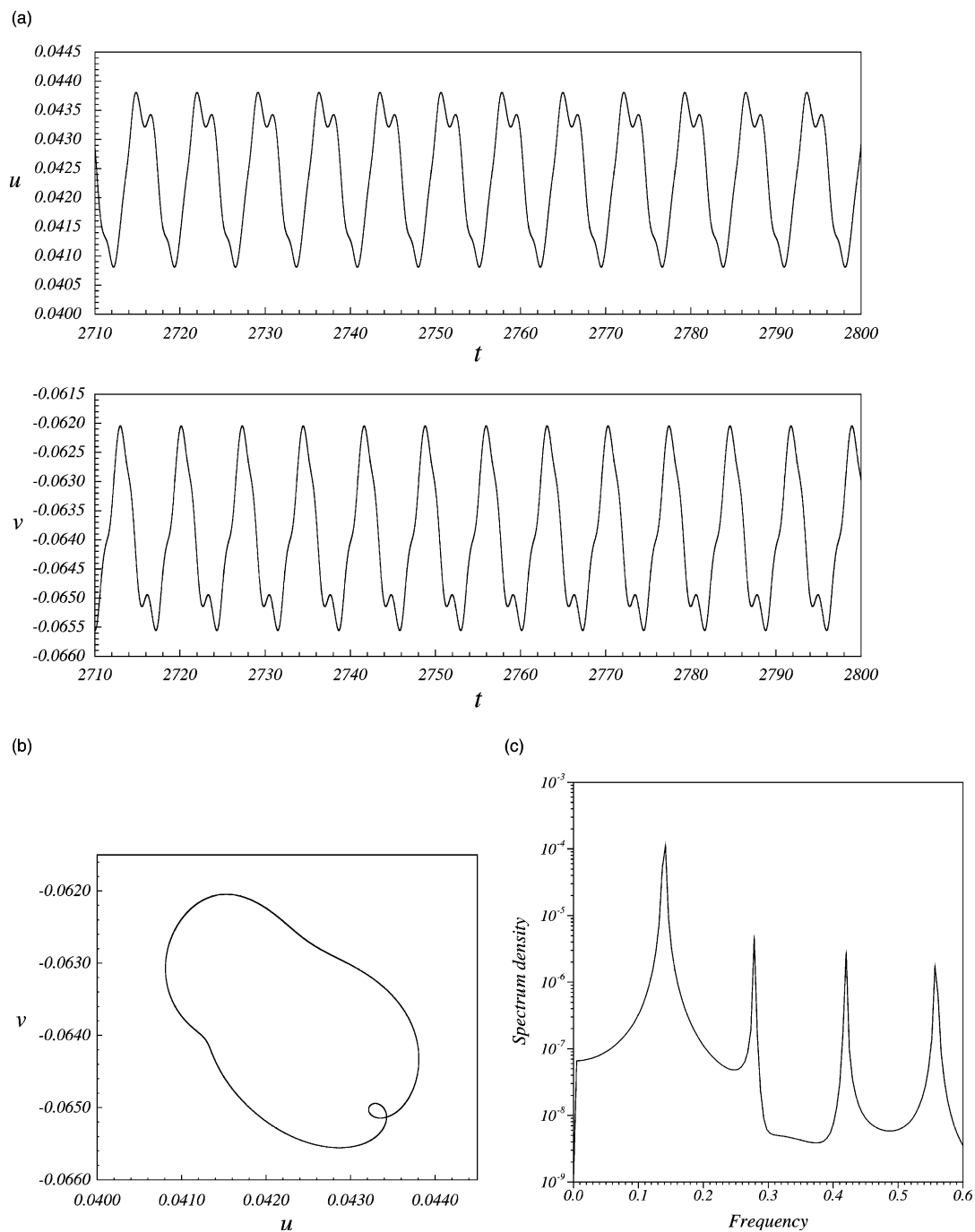


Fig. 8. Computed cavity flow at $Re = 10,600$ (BIIP1P). (a) u and v velocities as a function of time t (from $t = 2710$ to $t = 2800$). (b) Phase-space trajectories of v vs. u . (c) Fourier power spectra of the u velocity.

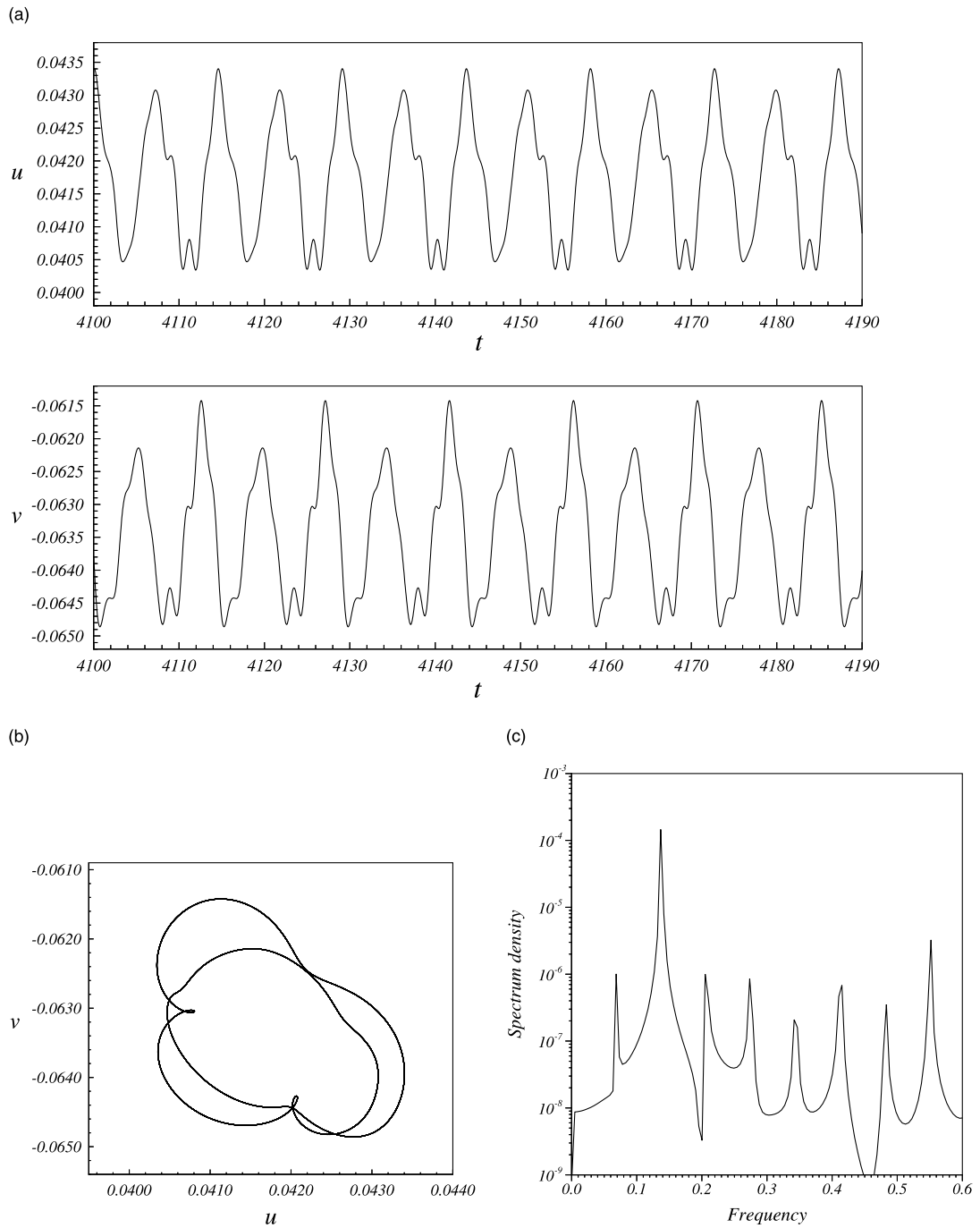
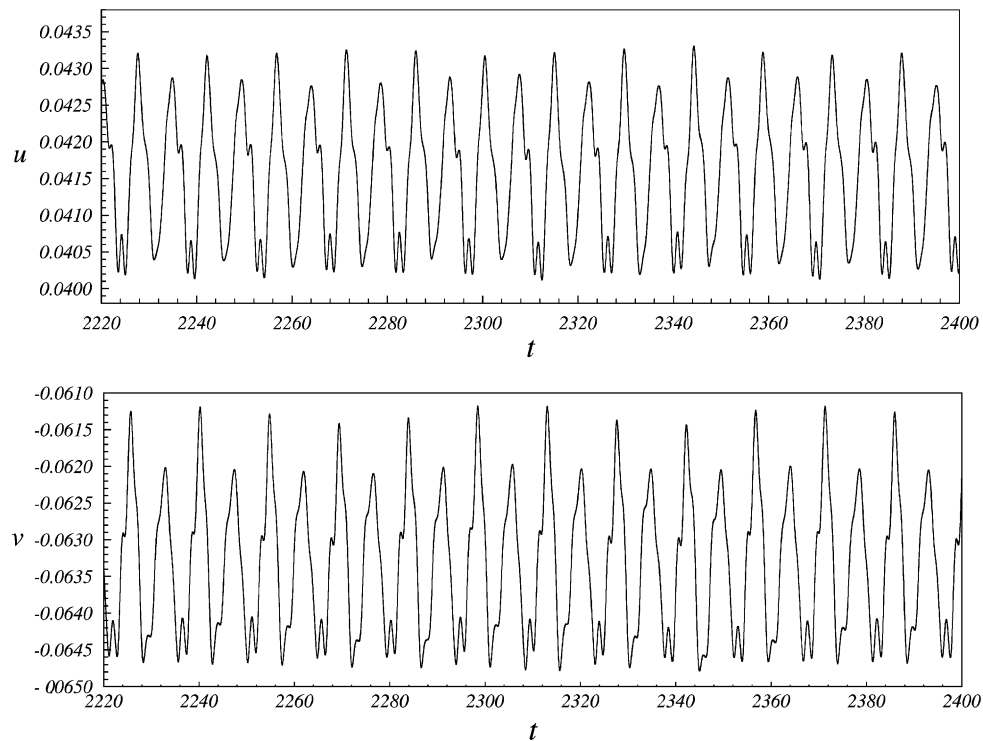
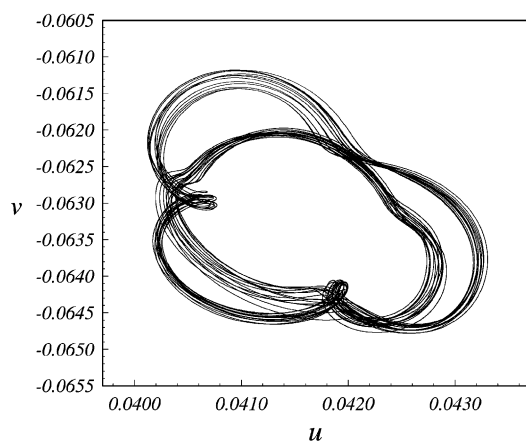


Fig. 9. Computed cavity flow at $Re = 10,900$ (BIIP2P). (a) u and v velocities as a function of time t (from $t = 4100$ to $t = 4190$). (b) Phase-space trajectories of v vs. u . (c) Fourier power spectra of the u velocity.

(a)



(b)



(c)

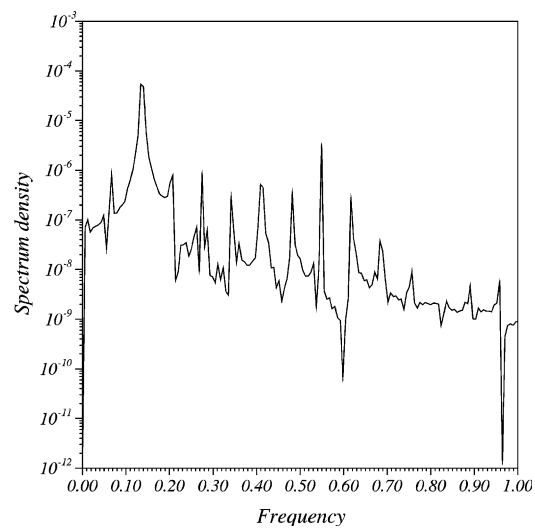


Fig. 10. Computed cavity flow at $Re = 11,000$ (chaotic). (a) u and v velocities as a function of time t (from $t = 2220$ to $t = 2400$). (b) Phase-space trajectories of v vs. u . (c) Fourier power spectra of the u velocity.

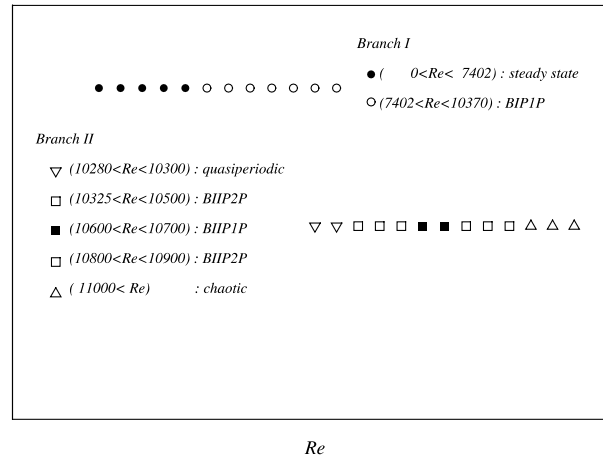


Fig. 11. A plot of the schematic description about the complex transition in lid-driven cavity flow.

Ruelle–Takens–Newhouse scenario for period-2 to quasi-periodic pattern. Besides, coexistence of two different patterns can be found at the same Re , i.e., bistability.

5. Conclusions

We have studied the transition from laminar to chaotic flow in the 2-D lid-driven cavity numerically, and we have found many interesting phenomena. These include the transition from the laminar to the periodic flow via supercritical Hopf bifurcation, the discontinuous transition from BIP1P to BIIP2P or from quasi-periodic pattern to BIIP2P, and the transition from BIIP1P to BIIP2P via period doubling which finally route to chaotic pattern. The discontinuous transition separates the whole solutions from laminar to chaotic flows in lid-driven cavity into two branches. It is quite obvious to see that laminar flow and chaotic flow belong to different branches in Fig. 11. These two branches with different FFs are verified by Fourier spectra. To the best of our knowledge, this is the first article to present the two-branches solutions of transition in the lid-driven cavity flow. The present result turns out that the theoretical treatment by Cazemier et al. [23] is not suitable in this case because the chaotic structure does not cover all phenomena with different dynamical characteristics.

Acknowledgements

This work was supported by the National Science Council under contract NSC88-2611-E-001-001, NSC90-2211-E-260-001 and the Institute of Physics, Academia Sinica, Taiwan, Republic of China.

References

- [1] Ruelle D, Takens F. On the nature of turbulence. *Commun Math Phys* 1971;20:167–92.
- [2] Newhouse S, Ruelle D, Takens F. Occurrence of strange axiom A attractors near quasiperiodic flow on T^m , $m \geq 3$. *Commun Math Phys* 1978;64:35–40.
- [3] Feigenbaum MJ. The transition to a periodic behavior in turbulent systems. *Commun Math Phys* 1980;77:65–86.
- [4] Manneville P, Pomeau Y. Different ways to turbulence in dissipative dynamical systems. *Physica D* 1980;1:219–26.
- [5] Gollub JP, Benson SV. Many routes to turbulent convection. *J Fluid Mech* 1980;100:449–70.
- [6] Giglio M, Musazzi S, Perini U. Transition to chaotic behavior via a reproducible sequence of period-doubling bifurcations. *Phys Rev Lett* 1981;47:243–6.
- [7] Gollub JP, Swinney HL. Onset of turbulence in a rotating fluid. *Phys Rev Lett* 1975;35:927–30.
- [8] Gorman M, Reith LA, Swinney HL. Modulation patterns, multiple frequencies, and other phenomena in circular Couette flow. *Ann New York Acad Sci* 1980;357:10–9.
- [9] McLaughlin JB, Orszag SA. Transition from periodic to chaotic thermal convection. *J Fluid Mech* 1982;122:123–42.
- [10] Orszag SA, Kells LC. Transition to turbulence in plane Poiseuille flow and plane Couette flow. *J Fluid Mech* 1980;96:159–205.
- [11] Orszag SA, Patera AT. Secondary instability of wall-bounded shear flows. *J Fluid Mech* 1983;128:347–85.
- [12] Ghaddar NK, Korczak KZ, Mikic BB, Patera AT. Numerical investigation of incompressible flow in grooved channel. Part I. Stability and self-sustained oscillations. *J Fluid Mech* 1986;163:99–127.
- [13] Amon CH, Patera AT. Numerical calculation of stable three-dimensional tertiary states in grooved-channel flow. *Phys Fluids* 1989;1:2005–9.
- [14] Burggraf OR. Analytical and numerical studies of the structure of steady separated flows. *J Fluid Mech* 1966;24:113–51.
- [15] Ghia U, Ghia KN, Shin CT. High- Re solutions for incompressible flow using the Navier–Stokes equations and a multigrid method. *J Computat Phys* 1982;48:387–411.
- [16] Schreiber R, Keller HB. Driven cavity flows by efficient numerical techniques. *J Computat Phys* 1983;49:310–33.
- [17] Thompson MC, Ferziger JH. An adaptive multigrid technique for the incompressible Navier–Stokes equations. *J Computat Phys* 1989;82:94–121.
- [18] Felice G, Denaro FM, Meola C. Multidimensional single-step vector upwind schemes for highly convective transport problems. *Numer Heat Transf, Part B* 1993;23:425–60.
- [19] Hou S, Zou Q, Chen S, Doolen G, Cogley AC. Simulation of cavity flow by the lattice Boltzmann method. *J Computat Phys* 1995;118:329–47.
- [20] Botella O, Peyret R. Benchmark spectral results on the lid-driven cavity flow. *Comput Fluids* 1998;27:421–33.
- [21] Poliashenko M, Aidun CK. A direct method for computation of simple bifurcations. *J Computat Phys* 1995;121:246–60.
- [22] Nobile E. Simulation of the time-dependent flow in cavities with the additive-correction multigrid method. Part II: Applications. *Numer Heat Transf, Part B* 1996;30:351–70.
- [23] Cazemier W, Verstappen RWCP, Veldman AEP. Proper orthogonal decomposition and low-dimensional models for driven cavity flows. *Phys Fluids* 1998;10:1685–99.
- [24] Ladyzhenskaya OA. *Mathematical problems in the dynamics of a viscous incompressible flow*. New York: Gordon and Breach; 1963.
- [25] Patankar SV. *Numerical heat transfer and fluid flow*. New York: McGraw-Hill; 1980.
- [26] Abdallah S. Numerical solution for the incompressible Navier–Stokes equations in primitive variables using a non-staggered grid, II. *J Computat Phys* 1987;70:193–202.
- [27] Harlow FH, Welch CH. Numerical calculation of time-dependent viscous incompressible flow of fluid with free surface. *Phys Fluids* 1965;8:2182–98.
- [28] Tamura T, Kuwahara K. Numerical study of aerodynamic behavior of a square cylinder. *J Wind Engng Ind Aerodyn* 1990;33:161–70.
- [29] Wissink JG. DNS of 2D turbulent flow around a square cylinder. *Int J Numer Meth Fluids* 1997;25:51–62.
- [30] Tafti D. Comparison of some upwind-biased high-order formulations with a second-order central-difference scheme for time integration of the incompressible Navier–Stokes equations. *Comput Fluids* 1996;25:647–65.